TU Delft

Delft University of Technology

Electrochemical evaluation of corrosion inhibiting layers formed in a defect from lithium-leaching organic coatings

Visser, P.; Meeusen, Mats; Gonzalez Garcia, Yaiza; Terryn, Herman; Mol, Arjan

DOI
10.1149/2.1411707jes

Publication date
2017

Document Version
Accepted author manuscript

Published in
Electrochemical Society. Journal

Citation (APA)
Visser, P., Meeusen, M., Gonzalez Garcia, Y., Terryn, H., & Mol, A. (2017). Electrochemical evaluation of corrosion inhibiting layers formed in a defect from lithium-leaching organic coatings. *Electrochemical Society. Journal*, *164*(7), C396-C406. https://doi.org/10.1149/2.1411707jes

Important note
To cite this publication, please use the final published version (if applicable).
Please check the document version above.

Copyright
Other than for strictly personal use, it is not permitted to download, forward or distribute the text or part of it, without the consent of the author(s) and/or copyright holder(s), unless the work is under an open content license such as Creative Commons.

Takedown policy
Please contact us and provide details if you believe this document breaches copyrights.
We will remove access to the work immediately and investigate your claim.

This work is downloaded from Delft University of Technology.
For technical reasons the number of authors shown on this cover page is limited to a maximum of 10.

This is an Accepted Author Manuscript of an article published by the ECS in the Journal of The Electrochemical Society, available online: http://dx.doi.org/10.1149/2.1411707jes

Electrochemical evaluation of corrosion inhibiting layers formed in a defect from lithium-leaching organic coatings

Peter Visser[a,b]*, Mats Meeusen[a], Yaiza Gonzalez-Garcia[a], Herman Terryn[a,c], Johannes M.C. Mol[a]

[a] *Delft University of Technology, Department of Materials Science and Engineering, Mekelweg 2, 2628 CD, Delft, The Netherlands*

[b] *AkzoNobel, Specialty Coatings, Rijksstraatweg 31, 2171 AJ, Sassenheim, The Netherlands.*

[c] *Vrije Universiteit Brussel, Research Group of Electrochemistry and Surface Engineering (SURF), Pleinlaan 2,1050, Brussels, Belgium*

** Contact author: +31 71 308 2789, p.visser-1@tudelft.nl*

Abstract

This work presents the electrochemical evaluation of protective layers generated in a coating defect from lithium-leaching organic coatings on AA2024-T3 aluminum alloys as a function of neutral salt spray exposure time. Electrochemical impedance spectroscopy was used to study the electrochemical properties on a macroscopic scale. An electrochemical model allowed to quantitatively link the electrochemical behavior with the physical model of the layer in the damaged area as studied by scanning electron microscopy. Local potentiodynamic polarization curves obtained from micro-cell measurements showed an increase of the passive range in the defect area due to the formation of a robust protective layer. Scanning vibrating electrode technique measurements confirmed the non-reversible long-term corrosion protection of these generated layers in the coating defect.

KEYWORDS: aluminum, coating, lithium, leaching, inhibition, corrosion

1. Introduction

In 2010, lithium salts were introduced as possible alternative to chromates as leachable corrosion inhibitor from organic coatings by Visser and Hayes(1). It was found that organic coatings loaded with lithium salts demonstrated effective corrosion inhibition in a defect under neutral salt spray (NSS) conditions. Further investigations revealed that under NSS corrosive conditions lithium salts leached from the organic coating into an artificial defect and increased the pH in the defect to values between 9 and 10(2). Under these alkaline conditions a hydrated aluminum oxide layer is formed in the defect area with a final thickness of 0.5-1.5 µm after 168 h NSS exposure. The protective layer has a typical physical morphology consisting of a dense barrier layer at the aluminum interface, a porous middle layer and a columnar outer layer(3). NSS testing according to aerospace standards demonstrated that this protective layer provides long-term corrosion protection comparable with chromate based inhibitor technology(4). X-ray photoelectron spectroscopy (XPS) indicated that the formed layers have the characteristics of a hydrated aluminum oxide like (pseudo)boehmite(2).

Protective aluminum oxide/hydroxide layers have been of interest since the late 1950s. It was reported at that time that the native aluminum oxide film is hydrated to form pseudoboehmite and boehmite upon immersion in water at elevated temperatures(5). Alwit and Kudo(6, 7) studied the formation of these pseudoboehmite layers at 50-100°C and prepared TEM cross-sections demonstrating a duplex structure with a dense inner layer and a porous outer layer. Buchheit et al.(8) studied protective layers prepared by a chemical conversion process from alkaline lithium salt solutions and demonstrated good corrosion protection on several aluminum alloys. Such conversion coatings showed clearly a two-layer morphology comprising a thin

amorphous inner layer and an outer crystalized hydrotalcite layer(9). Din et. al. generated boehmite layers with a similar duplex morphology with the accelerated oxide film growth method, using steam(10). In their work, they demonstrated that these layers provide corrosion protection on AA6060 alloys by electrochemical analysis and standard corrosion testing such as acid assisted salt spray and filiform corrosion resistance. Potentiodynamic polarization measurements showed a reduction in anodic and cathodic activity and the pitting potential shifted to more noble values(11).

While our previous studies focused on the structure, morphology, and formation of the protective hydrated aluminum oxide layer in a defect, the development of the electrochemical response of these layers over time has not yet been studied (2, 4, 12, 13). Therefore, the aim of this work is to study the development of the electrochemical characteristics and to link these with the physical properties of the protective layer during and after its formation in an artificial coating defect on AA2024-T3, using field emission scanning electron microscopy (FESEM) and (local) electrochemical techniques. To this aim, artificially damaged lithium-leaching organic model coatings applied on AA2024-T3 aluminum alloys were exposed to a neutral salt spray corrosion test (ASTM B-117). Cross-sectional analysis of the defect area using FESEM showed the thickness evolution and morphological formation of the protective layer over time. The evolution of the electrochemical response of the layer in the defect area was studied as a function of time using a combination of (local) electrochemical techniques. Electrochemical impedance spectroscopy (EIS) was used for the quantification of the electrochemical characteristics of the hydrated aluminum oxide in the coating defect on a macroscopic scale. Local potentiodynamic polarization measurements in an electrochemical micro-cell arrangement were

performed to determine the passive range and breakdown potential of the generated layers in the defect area on a microscopic scale. Scanning vibrating electrode technique (SVET) measurements were performed to investigate the electrochemical stability of the formed layer after NSS exposure. This dedicated combination of electrochemical techniques provides pivotal information on the electrochemical and physical development of the layer in a coating defect aimed to develop our insights into the corrosion protective properties of these lithium-leaching organic coatings.

2. Experimental

Materials

Polyurethane model coatings with a composition as listed in Table 1 were used for this work. The lithium-salt loaded coatings have a total pigment volume concentration (PVC) of 30 vol %, comprising 15 vol % inorganic pigments and fillers and 15 vol % lithium salt respectively. Analytical grade lithium carbonate and lithium oxalate purchased from Sigma Aldrich were used as lithium-leaching compounds for active inhibition.

Sample preparation

The pigmented organic coatings were prepared according to the following procedure. The raw materials of Component A were added sequentially while stirring into a 370 ml glass jar. Subsequently, 400 grams Zirconox® pearls (1.7 - 2.4 mm) were added to the mixture for grinding and dispersion of the pigments. The samples were shaken for 20 minutes on a Skandex® paint shaker to achieve a fineness of grind less than 25 µm. After shaking the pearls were separated from the coating. Component B was added separately, and the paint was stirred to a

homogeneous mixture.

AA2024-T3 bare aluminum alloy (Alcoa) was anodized in tartaric-sulfuric acid (TSA) according to aerospace requirements (AIPI 02-01-003). The model coatings were applied with a high volume low pressure (HVLP) spray gun at ambient conditions (23°C and 55 % RH). After the application and a 1 h flash-off period, the coated panels were cured at 80°C for 16 h. The dry film thickness of the coatings after drying was 20-25 μm.

An artificial damage was made on the coated panels with a mechanical milling device leaving a U-shaped scribe of 1 mm wide and 100-150 μm deep. After scribing, the samples were exposed to the neutral salt spray test (ASTM-B117) for varying periods of time, from 2 h up to 168 h. Before each sample analysis, the corrosion process was quenched and any residual chlorides were removed by rinsing the panels with flowing deionized water for 2 min and air-drying.

Scanning electron microscopy (SEM)

Cross-sectional observations of the scribed region were carried out using a JEOL JSM-7100F field emission SEM using the backscatter electron detector (BED-C) at 5 kV and a working distance of 3 mm. The samples were sectioned using a diamond saw and consecutively ion milled using a Hitachi IM4000 ion milling system at 6kV Ar-ion acceleration, a 3 times-per-minute sample rotation speed and a swing angle of +/- 30º.

Electrochemical impedance spectroscopy (EIS)

The electrochemical behaviour of coated AA2024-T3 samples in the presence of a coating defect was studied with EIS before and after different periods of neutral salt

spray (NSS) exposure. EIS measurements were performed at OCP using a Gamry Interface 1000 computer-controlled potentiostat over a frequency range from 10^{-2} Hz to $3 \cdot 10^{4}$ Hz, 7 points per decade and a sinusoidal amplitude of 10 mV, using a three-electrode set-up in a Faraday cage, equipped with a saturated calomel electrode (SCE) as the reference electrode, platinum wire as the counter electrode and a scribed panel as the working electrode using a 0.05 M NaCl electrolyte. The area exposed to the electrolyte was 12.5 cm^2, the effective bare electrode (i.e. the coating defect) area was 0.48 cm^2 and the volume of electrolyte was 60 cm^3. Measurements were recorded after 4 to 8 hours exposure to the 0.05M NaCl electrolyte on at least three samples for each exposure condition. The impedance plots were fitted using different equivalent circuits with Zview from Scribner Associates Inc.

Electrochemical micro-cell technique

The micro-cell technique was used for local potentiodynamic polarization measurements. The polarizations were performed using the equipment set-up as developed by Suter and Böhni(14). A micro-capillary with an internal diameter of about 100 µm was selected to perform the measurements in the (scribed) defect area. This capillary diameter corresponds to an exposed sample area of about $7.85 \cdot 10^{-5}$ cm^2. The capillary was pulled with a Sutter Instruments micro-pipette puller followed by grinding and polishing it to the required size. Before use, a deformable hydrophobic silicone gasket was prepared at the end of the micro-capillary tip. The set-up of the cell comprised a three-electrode configuration: the sample scribe area as working electrode; a Pt-counter-electrode and an Ag/AgCl 3M KCl reference electrode. The measurements were controlled by a high resolution Jaissle IMP83 PCT-BC potentiostat. The anodic potentiodynamic scans were performed at a scan rate of 1

mVs^{-1}, starting -50 mV from the open circuit potential (OCP) and 5-10 minutes after the micro-capillary was positioned on the surface in the scribe. All experiments were performed in 0.05 M NaCl aqueous solution. For each exposure time at least 3 measurements were taken to ensure reproducibility.

Scanning Vibrating Electrode Technique (SVET)

The electrochemical stability of the protective layer in the coating defect area has been investigated using a SVET instrument from Applicable Electronics Inc. controlled with ASET software from ScienceWares Inc. Current density maps were recorded by scanning the Pt-Ir vibrating micro-electrode over a defect in the coating. A defect, penetrating the coating into the AA2024-T3 substrate (1.3 mm diameter and about 150 μm deep), was made with a flat-bottom drilling bit using a Gravograph engraving machine. The lithium-leaching coatings with the defect were exposed to 168 h NSS exposure. Following the exposure the samples were immersed in the 0.05 M NaCl electrolyte and SVET current density maps were recorded up to 14 days immersion. The SVET probe was located at 100 μm from the coating around the defect and as a result the tip-defect bottom distance is 200-250 μm. The dimensions of the SVET maps were around 1700 × 1700 μm using 41x41 points per map.

3. Results and discussion

3.1 Visual and microscopic coating defect analysis as a function of NSS exposure time

In the aerospace industry, the active protective properties of coatings are tested by means of neutral salt spray (NSS) exposure according to ASTM B-117(15). Prior to exposure, an artificial defect is made through the coating into the metal and the degree of corrosion is assessed after various periods of exposure. Fig.1a-d shows the rapid formation of corrosion products in such a defect when exposed to corrosive conditions as a function of time in case a coating has no inhibitive capabilities for protection of AA2024-T3 bare aluminum alloy. The first signs of corrosion are evident after only 2 h of exposure (Fig. 1a) illustrating the intrinsic high corrosion susceptibility of the AA2024-T3 alloy. The corrosion continues with time and results in a large amount of voluminous corrosion products in the scribe after 48 and 168 h of exposure (Fig. 1c and d). In contrast to the coating without corrosion inhibitor, both model coating formulations, loaded with lithium carbonate (Fig. 1e-h) and lithium oxalate (Fig. 1i-l) as leachable corrosion inhibitor, showed no corrosion products in the scribed area after 168 h of NSS exposure. This demonstrates the effective active protective properties of these lithium-based inhibitor loaded coatings. Fig. 2 shows micrographs of cross-sections of defect areas before and after NSS exposure. Fig. 2a shows the general overview of the cross-sectional edge region of the defect prior to exposure. Fig. 2b shows the typical surface of the unexposed scribe bottom. Fig 2c shows the cross-sectional edge region of the defect in case lithium-leaching coatings are applied and exposed to NSS after 168 h of exposure. The cross-sectional micrographs of a coating defect of a lithium oxalate loaded coating covered samples confirm the absence of corrosion and reveal the protective layer that was formed throughout the scribed area. Fig 2d shows the typical morphology of the hydrated aluminum oxide layer that is formed from this lithium oxalate loaded coating covered sample under these corrosive conditions(3). The layer covers the entire surface of the

damaged alloy. This characteristic layer is formed rapidly from the lithium-leaching coating technology and protects the damaged area effectively.

3.2 Protective layer formation as a function of NSS exposure time

To study the formation and the characteristics of the protective layer in the defect area over time, ion-milled cross-sections of lithium carbonate and lithium oxalate loaded coatings were analyzed after 2, 8, 48, and 168 h of NSS exposure. Fig. 3 shows cross-sectional micrographs of the protective layer during its formation over this period of time. The micrographs show that after 2 h NSS exposure a layer of 0.3 to 0.5 µm has been formed on the aluminum surface of the scribe. (Fig. 3 a,e). The layer has a dense morphology at the aluminum metal/oxide interface of ~ 0.1 µm and a more porous morphology at the outer surface. As result of longer exposure, the layer develops in thickness and morphology on the outer side. After 8 to 48 h of exposure, the layer thickness varies between 0.6-0.8 µm and both the lithium carbonate and lithium oxalate loaded samples shows the development of a columnar structure at the outer surface and maintaining a dense layer at the aluminum interface (~0.1 µm) (Fig. 3b and f, 8 h; Fig 3. c and g, 48 h). After 168 h the protective layers have grown to a thickness of about 1.0-1.2 µm and show the characteristic morphology of a dense inner layer (~0.1 µm), a porous middle layer and a columnar outer layer as observed in our previous studies (4). It is important to notice that the thickness of the dense inner layer remains similar, ~0.1 µm, for both lithium-leaching coatings for the full exposure time of 168 h. Fig. 4 shows the quantitative development of the thickness of the layer derived from the micrographs of the cross-sections. It can be noted that after 2 and 8 h NSS exposure, the thickness of the layers from the lithium oxalate loaded

coating are thicker compared to the layers generated from the lithium carbonate loaded coatings. This can be explained by the lower initial pH in the defect area of the lithium oxalate coatings as observed by local pH measurements in previous work(2). The development of the aluminum hydroxide gel layer is a result of the competitive film formation process of chemical dissolution at aluminum hydroxide gel/solution interface and film growth at the metal/ aluminum hydroxide gel interface. This in line with the results of Hurlen and Haug, who observed that thickness of the layer is related to the pH of the solution. A higher pH accelerates the chemical dissolution at the aluminum hydroxide gel/solution interface resulting in thinner layers(16, 17).

The results confirm the previously proposed multistep-process to comprise basically 4 steps(2): oxide thinning, anodic dissolution, formation of an aluminum hydroxide gel layer, and finally the aging of this gel into a hydrated aluminum oxide(17, 18). The cross-sections revealed the formation of the protective aluminum hydroxide gel on the alloy in the early stages, followed by the ageing process resulting in the characteristic three-layered morphology of the protective layer with a dense layer at the aluminum interface, a porous transition layer in the middle and a columnar morphology at the top.

3.3 Corrosion protective properties as a function of NSS exposure time

EIS measurements

The electrochemical characteristics of the layers formed in a defect from coatings with and without lithium-leaching compounds were measured by EIS. Fig. 5 shows the Bode plots of the coatings with and without lithium-leaching compounds after 168 h NSS exposure. A non-exposed reference sample was measured to show the initial

state of the scribe (damaged area) representing the alloy with a native oxide. After exposure to the corrosive NSS conditions, the Bode plots of the impedance modulus (Fig. 5a) of both lithium-leaching coatings show an increase of impedance values in the middle frequency (10^{1}-10^{3} Hz) and low frequency (10^{-1}-10^{-2} Hz) ranges compared to the unexposed sample and the sample without inhibitor. This increase of the impedance modulus in the middle frequency range can be associated with the formation of an (oxide) layer in the damaged area(19). The increase of the impedance modulus at low frequencies by approximately one order of magnitude can be associated with the increased corrosion resistance of the layers generated from the lithium-leaching coatings(20). The accompanying phase angle plots of these measurements are shown in Fig. 5b. In case of the unexposed scribe the phase angle diagram shows clearly two time-constants, one at 10^{1} Hz for the thin oxide layer and one at 10^{-1} Hz related to the electrochemical activity at the aluminum interface in the coating defect, which are characteristic for the native oxide on aluminum(21). After NSS exposure, the Bode phase angle diagram of the coating without inhibitor shows still two time-constants. However, the time-constant at the middle frequency shifted to a lower frequency and the second time-constant at the low frequency increased slightly. This behavior can be explained due to the formation of corrosion products in the defect area. The Bode phase angle plots for both lithium-leaching coatings show a broadening of the phase angle around 10^{1} – 10^{3} Hz as a result of the generated layer in the defect area. It can be noted that this phase angle peak has an asymmetric shape and shows a shoulder in the higher frequency area around 10^{2} to 10^{3} Hz. This asymmetry suggests that there are possibly two overlapping time-constants in this frequency range. The phase angle of the time-constant observed at the low frequency

range (10^{-1}Hz) has increased. This increase of the phase angle in the low frequency range can be associated with an improved corrosion protection.

Fig. 6 shows the Bode plots representing the behavior of the impedance of the samples with and without lithium-leaching coatings before and after the various exposure times in the NSS. The coating without inhibitor (Fig. 6a and d) shows a decrease of the impedance in the mid frequency range and the time-constant shifts to lower frequencies over time. This phenomenon can be explained by the dissolution of the native oxide. When analyzing the Bode impedance modulus plots of the lithium-leaching coatings (Fig. 6b and c) it can be noticed that impedance modulus values increase almost instantaneously for both samples due to the NSS exposure. After only 2 h NSS exposure, the impedance modulus values have increased significantly in the middle and low frequency range and increased further as a result of longer exposure times. After 168 h the impedance modulus reaches a maximum. Compared to the sample with the native oxide, the impedance modulus of the hydrated aluminum oxide layer increased by about one order of magnitude in the low frequency range and increased a half order of magnitude in the middle frequency range. The lithium carbonate and lithium oxalate coatings show similar protective behavior independent of the anion used. The Bode phase angle plots of the lithium-leaching coatings are shown in Fig. 6d and e. It can be noted that the phase angle of the respective time-constants increased and broadened as a result of the NSS exposure time. Overall, this indicates that the electrochemical characteristics can be linked with the formation of the protective layer as observed in the FESEM cross sections (Fig. 3)

The EIS spectra of these measurements were fitted with equivalent circuits (ECs) to quantitatively describe the electrochemical properties of the generated layers in the

defect during the formation(22). Fig. 7 shows the two equivalent circuit models used to fit the data from the EIS measurements. EC1, a two time-constant circuit, was used to describe the effect in the defect of a damaged coating without inhibitor prior and after NSS exposure. R_{sol} represents the resistance of the electrolyte; R_{oxide} is the resistance of the (native) oxide layer and the CPE_{oxide} is the constant phase element (CPE) describing the capacitance of the oxide layer using parameters Q_{oxide} and n_{oxide}, the electrochemical processes at the aluminum interface are represented by R_{pol} and CPE_{dl}. R_{pol} is the polarization resistance and CPE_{dl} is accounting for the double layer capacitance. CPE's are commonly used to describe the frequency dependence of elements with a non-ideal capacitive behavior(23). In this work, CPE is used to account for the dispersive behavior of the time-constants due to the non-uniformity of the layers generated in the defect(2, 12).

An equivalent circuit model (EC2) with three time-constants was used for the fitting of the EIS spectra of the lithium-leaching samples. The physical morphology of the protective hydrated aluminum oxide layer observed in the defect by FESEM and represented by the Bode phase angle plots (Fig. 6e and f) indicate that a three time-constant equivalent circuit model (EC2) is more appropriate compared to the two time-constant model (EC1). The metal/oxide layer interface and dense barrier layer are represented by two clearly defined time-constants at the low ($5 \cdot 10^{-2} - 10^{-1}$ Hz) and middle (10^{1}-10^{3} Hz) frequency range respectively. The third time-constant of EC2 describes the contribution of the broader phase angle at the higher frequencies (10^{2} - 10^{3} Hz) related to the porous outer layer. EC2 can be interpreted as: R_{sol} for the solution resistance, R_{porous} and CPE_{porous} describe the contribution of the porous middle layer, R_{oxide} and CPE_{oxide} represent the dense inner layer, and CPE_{dl} and R_{pol} describe the double layer capacitance and polarization resistance at the metal/oxide

interface. The fitted curves are displayed as solid lines in the Bode plots of Fig. 6. The numerical values of the fittings from these spectra are listed in Table 2, 3 and 4.

The results for the coating without inhibitor (Table 2) showed an initial decrease of R_{oxide} followed by a gradual increase. This behavior could indicate the process of oxide thinning followed by the precipitation of the corrosion products in the defect area. Table 3 and 4 show the fitting results of the lithium-leaching coatings. The most important observation from these data is the significant increase of R_{oxide} and R_{pol} over time for both coatings related to the generation of a dense oxide layer at the aluminum interface. R_{oxide} increases by a factor 7 and 10 for the lithium carbonate and lithium oxalate loaded coatings respectively. In addition, the polarization resistance increased by a factor 20 for the lithium carbonate loaded coating and a factor 10 for the lithium oxalate loaded coating compared to the native oxide and the coating without inhibitor.

For further analysis and comparison, the equivalent capacitance of the different elements in the equivalent circuit was calculated using the CPE parameters (Q and n) and the resistance corresponding to each time-constant using the equation:

$$C = R^{\frac{(1-n)}{n}} Q^{\frac{1}{n}} \quad (1)$$

This is equation is applicable to a normal time-constant distribution through a surface layer according to Hirschorn et al.(24). The resistance and capacitance of the dense oxide layer (R_{oxide} and C_{oxide}) and the metal/oxide interface (R_{pol} and C_{dl}) was calculated from at least 3 replicate measurements. Fig. 8 shows the evolution and scatter of the resistance and capacitance of the oxide layer and the metal/oxide interface as a function of NSS exposure time. Fig. 8a shows that resistance of the oxide (R_{oxide}) increased over time due to the formation of the dense layer from the lithium-leaching coatings. Whereas the defect area has a R_{oxide} of about 3.7 kΩ cm^2

before NSS exposure, the resistance almost tripled after only 2 h NSS exposure. Over prolonged exposure, R_{oxide} shows a gradual increase to values of 25-30 kΩ cm^2 after 168 h (Fig. 8a). At the same time, the capacitance of the formed dense layer (C_{oxide}) is reduced by a factor 5 lower after 2 h NSS exposure compared the native oxide and remains stable over time around 20-30 µF/cm^2 (Fig. 8c). This behavior can be related to the rapid formation of the dense layer on the substrate and a gradual further densification and reducing porosity increasing the oxide resistance while maintaining its thickness as reflected by the FESEM cross-sectional analysis in Fig. 3. The resistance of the oxide (R_{oxide}) of the coating without inhibitor remains at a level of 5 to 9 kΩ cm^2. In addition, the oxide capacitance of the coating without inhibitor is increasing rapidly indicating degradation of the oxide layer (inset Fig. 8c). The corrosion activity at the substrate can be characterized by the time-constant consisting of the polarization resistance (R_{pol}) and the double layer capacitance (C_{dl}). Fig. 8b and d show the evolution of the R_{pol} and C_{dl} during the formation of the protective layer in the defect. Compared to the defect prior to NSS exposure, both lithium-leaching coatings show increasing polarization resistance (Fig. 8b) and decreasing double layer capacitance (Fig. 8d) over time indicating improved corrosion protective properties of the formed layer on the aluminum in the defect area. For the coatings without inhibitor the polarization resistance (R_{pol}) remained around the initial level and the double layer capacitance (C_{dl}) increased to very large values (inset Fig. 8d), indicating the presence of the corrosion process. The observed trend of increasing resistances and decreasing capacitances of the lithium-leaching coatings is consistent with the formation and densification of the protective layer in the defect area. The observed effect corresponds with the trend of increasing layer thickness over time in Fig. 4.

The inhibition efficiency (IE) of the generated layers in the defect was calculated from the impedance data at the various intervals using the following equation(25, 26):

$$IE\ (\%) = \frac{R_{pol\ (lithium)} - R_{pol\ (no\ inhibitor)}}{R_{pol\ (lithium)}} \times 100\% \qquad (2)$$

where $R_{pol(lithium)}$ represents the polarization resistance of the protective layer generated from a lithium-leaching coating and $R_{pol(no\ inhibitor)}$ represents the polarization resistance in the defect from a coating without inhibitor after the same NSS exposure time. The inhibiting efficiency of the layers generated in a defect area from lithium leaching coatings are shown in Fig. 9. The inhibition efficiency of the lithium carbonate loaded coating demonstrates an inhibiting efficiency of around 80% after only 2 hours which develops further up to 95% after 48 h and remains at a similar level upon longer exposure. The inhibition efficiency of the protective layer from the lithium oxalate loaded coating develops faster in the first hours this can be related to the faster layer thickness development of these lithium oxalate loaded coatings in Fig. 4. The development of the inhibition efficiency confirms the fast and effective inhibition provided by protective layers generated in the defect area.

Fig. 10 shows the schematic equivalent circuit that can be related with the physical morphology of the corrosion protective layer in the defect. Considering the physical morphology of the protective layers and the quantitative EIS results, it can be concluded that the improved corrosion protective properties of the formed layer can be attributed to the rapid formation of the dense and compact layer at the aluminum interface. The impedance part related from the porous part plays only a minor role in the overall corrosion resistance.

Electrochemical micro-cell measurements

Whereas EIS measurements provide averaged information on the electrochemical response of the protective layer in the coating defect over a large area, complementary information on a local scale was obtained using the electrochemical micro-cell technique. This technique provides the opportunity to perform potentiodynamic polarization measurements on the formed layer on a local area in the defect, using a micro-capillary. The micro-cell technique was used to correlate the local passivity (breakdown potential) of the protective layer with the morphology of the layer as observed with the SEM. Fig. 11 shows the anodic polarization curves of the protective layer generated in the scribe of the lithium-leaching coatings after different periods of neutral salt spray exposure. Cathodic polarization measurements were not considered since their interpretation can be misleading(27). The silicone gasket at the end of the micro-capillary is permeable to oxygen. This enables the diffusion of oxygen through the gasket, and may increase the oxygen reduction reaction and mask any diffusion control. Fig. 11a and b show that the polarization curve of the unexposed samples show that the native oxide has a breakdown potential of about + 0.15 V from the OCP. In contrast to this, the lithium-leaching coatings show a large passivity region with a shift of the breakdown potential to significantly more positive values. In Fig. 11a, the lithium carbonate loaded coating shows a shift of the breakdown potential to values from +0.9 up to +1.6 V. These values are already achieved after 2 h exposure and fluctuate over time. The same behavior is observed for the lithium oxalate loaded coatings (Fig. 11b). For this system the anodic passive range even exceeds +2.5 V from the OCP after 168 h exposure. Table 5 lists the average corrosion and breakdown potentials for the lithium-loaded coatings systems before and after exposure. It can be noted that there is some scatter for the corrosion potential and

breakdown potential. This scatter in electrochemical behavior measured with the local micro-cell technique can be related to the heterogeneous nature of both the aluminum alloy and the oxide layer as also observed by others in previous works(12, 28). For both lithium-leaching coatings, the polarization curves of the neutral salt spray exposed samples exhibit a large passive behavior compared to the unexposed scribe. However, in the case of the lithium oxalate loaded coatings, a more gradual increase in the average breakdown potential is observed, ranging from +0.4 V after 2 h exposure, and increasing to +0.9, +1.3 and +2.3 V versus OCP after 8, 48 and 168 h, respectively. This can indicate that the protective nature of the layer develops more gradually compared to the lithium carbonate loaded coating.

From these micro-cell measurements, we can conclude that the protective layers are formed quickly and they have a good stability and polarization resistance as shown by the passive anodic behavior and the increased breakdown potential. These results correspond rather well with the FESEM and EIS results, previously discussed. A similar passive behavior was observed by Din et. al.(11) who prepared corrosion protective layers with a similar structure on aluminum alloys by the steam assisted oxide growth method.

3.4 Stability of the protective layer as a function of NSS exposure time

It is essential that the generated protective layer has an irreversible nature and provides long term corrosion protection once formed. The Scanning Vibrating Electrode Technique (SVET) has been used to investigate the long-term resistance to electrochemical degradation of the generated protective layer in the defect. The SVET enables to monitor in situ the distribution and magnitude of local ionic currents over

an electrochemically active surface with µm-scale resolution within a mm-sized sample area. Fig. 12 shows the SVET maps and the corresponding optical images of the defects of the three systems: unexposed coating without inhibitor and the lithium-leaching coatings after 168 hours of exposure to NSS conditions. A sequence of SVET maps was obtained for each system at different immersion times in NaCl solution. Fig. 12a shows SVET maps corresponding to the unexposed coating without inhibitor. After initiation of the immersion, the map shows low current density values below 10 $\mu A \cdot cm^2$ and no clear evidences of corrosion activity. Optical image of the sample showed a pristine surface. After 24 h, local activity is observed in the SVET map. A localized anodic region was detected with maximum current density values of about 50 $\mu A \cdot cm^2$. Cathodic regions were observed next and close to the anodic area, with maximum current density values of around -50 $\mu A \cdot cm^2$. This activity is also confirmed by the optical image of the sample that showed indications of corrosion in the defect. After 7 days, SVET measurements were not possible due to the presence of voluminous corrosion products in the defect area. In the case of the lithium-leaching coatings, both, the lithium carbonate (Fig. 12b) as well as the lithium oxalate (Fig. 12c) systems showed SVET maps with very low anodic and cathodic current densities (less than 10 $\mu A \cdot cm^2$) up to 14 days exposure to the electrolyte. Furthermore, no corrosion products or pits are being formed in the defect area over time. In addition to the fast and effective formation of the protective layer in the defect, these SVET results demonstrate the irreversible nature of the corrosion resistance provided the hydrated aluminum oxide layer which is essential to ensure long-term corrosion protection.

3.5 Corrosion inhibition mechanism with lithium-leaching coatings

The results demonstrate that the corrosion inhibiting mechanism of these lithium-leaching coatings is fundamentally different compared to previously studied corrosion inhibitors. Corrosion inhibitors such as vanadates, cerium compounds, and organic inhibitors are known to inhibit by precipitation on the heterogeneous surface microstructure of AA2024-T3, hence preventing high microgalvanic activity(29-33). The inhibition mechanism of the lithium-leaching coatings differentiates itself from other inhibitor technologies by the spontaneous conversion of the surface of a damaged area with a relatively thick and stable hydrated aluminum oxide layer.

Although thicker and different in nature, the behavior of these protective layers is comparable to an anodic oxide layer or layers generated by chemically assisted hydrothermal sealing(22, 34). Oxides generated by these treatments also cover the entire aluminum interface with a duplex layer consisting of a dense inner barrier layer and porous outer layer but these are generally prepared in well-controlled solutions and need a considerable amount of energy(19, 35). There is no clear difference between the protective properties of the layers generated from the two different lithium-salts. Although, electrochemical and microscopy results indicate that the layers generated from the lithium oxalate loaded coatings are forming faster compared to the lithium carbonate loaded coating. However, there is not a significance difference in corrosion protection between the layers generated from both salts. These results combined with the previous results on the morphology of the layers(3), leaching behavior and pH development(2) provide more understanding about the processes during development and characteristics of the protective properties of these layers generated in the defect from lithium-leaching organic coatings. It must be noted that, due to the nature of the NSS exposure test, these experiments did not provide exact information about the lithium concentration needed to obtain this

degree of corrosion protection. More research is needed to investigate the role of lithium in this corrosion inhibiting mechanism in more detail.

4. Conclusions

The electrochemical characteristics of the corrosion protective layers generated in a coating defect from lithium-leaching coatings on AA2024-T3 aluminum alloys when exposed to neutral salt spray conditions over time were studied. The electrochemical properties were linked with the physical properties of the protective properties using microscopy and (local) electrochemical techniques. Effective corrosion inhibition from these lithium-leaching coatings was observed after NSS exposure. Cross-sectional microscopic analysis revealed the fast and effective growth of protective layers in thickness and morphology covering the entire damaged area. The complementary results obtained from (local) electrochemical techniques demonstrate the development of the corrosion resistant properties due to the generation of a protective layer in the defect area and this layer exhibits an irreversible long-term resistance to corrosive conditions. The corrosion protective properties of this layer can be attributed to the dense inner layer of the protective layer. There were no significant differences in corrosion protection observed between lithium carbonate and lithium oxalate salts. The results of this study confirm the fast and effective active protective nature of these lithium-leaching coatings.

5. Acknowledgements.

The authors would like to acknowledge Marc Raes for his assistance and help with the FE-SEM analysis, Francesco Andreatta (University of Udine, Italy) for providing training on the electrochemical micro-cell technique, Agnieszka Kooijman for her

assistance in performing the micro-cell measurements, Wilma Ravesloot and Lennaert Klerk of AkzoNobel for providing the ion-milled samples for this study. This research was carried out under the collaboration agreement between AkzoNobel and Delft University of Technology.

References

1. P. Visser and S. A. Hayes, WO2010112605-A1, in, p. a. o. a. a. Low-temperature-curable coating composition useful as anticorrosive primer coating for non-ferrous metal substrates, comprises film-forming resin, curing agent, and lithium salt Editor, p. 2414464, Akzo Nobel Coatings Int Bv (Alku) (2010).
2. P. Visser, A. Lutz, J. M. C. Mol and H. Terryn, *Progress in Organic Coatings,* 99, 80 (2016).
3. P. Visser, Y. Liu, X. Zhou, T. Hashimoto, G. E. Thompson, S. B. Lyon, L. G. J. van der Ven, A. J. M. C. Mol and H. A. Terryn, *Faraday Discussions,* 180, 511 (2015).
4. P. Visser, Y. Liu, H. Terryn and J. M. C. Mol, *Journal of Coatings Technology and Research,* 1 (2016).
5. R. K. Hart, *Transactions of the Faraday Society,* 53, 1020 (1957).
6. T. Kudo and R. S. Alwitt, *Electrochimica Acta,* 23, 341 (1978).
7. R. S. Alwitt, *Journal of the Electrochemical Society,* 121, 1322 (1974).
8. R. G. Buchheit, Bode, M.D., Stoner, G.E., *Corrosion,* 50, 205 (1994).
9. C. A. Drewien, Eatough, M.O., Tallant, D.R., Hills, C.R., Buchheit, R.G., *Journal of material research,* 11, 1507 (1996).
10. R. U. Din, V. C. Gudla, M. S. Jellesen and R. Ambat, *Surface and Coatings Technology,* 276, 77 (2015).
11. R. U. Din, K. Bordo, M. S. Jellesen and R. Ambat, *Surface and Coatings Technology,* 276, 106 (2015).
12. Y. Liu, P. Visser, X. Zhou, S. B. Lyon, T. Hashimoto, M. Curioni, A. Gholinia, G. E. Thompson, G. Smyth, S. R. Gibbon, D. Graham, J. M. C. Mol and H. Terryn, *Journal of The Electrochemical Society,* 163, C45 (2016).
13. Y. Liu, P. Visser, X. Zhou, S. B. Lyon, T. Hashimoto, A. Gholinia, G. E. Thompson, G. Smyth, S. R. Gibbon, D. Graham, J. M. C. Mol and H. Terryn, *Surface and Interface Analysis,* doi: 10.1002/sia.5972 (2016).
14. T. Suter and H. Böhni, *Electrochimica Acta,* 42, 3275 (1997).
15. P. Visser , H. A. Terryn and J. M. Mol, in *Active Protective Coatings, New-Generation Coatings for Metals,* 1 ed., A. E. Hughes, J. M. Mol, M. L. Zheludkevich and R. G. Buchheit Editors, p. 315, Springer, Netherlands (2016).
16. T. Hurlen and A. T. Haug, *Electrochimica Acta,* 29, 1133 (1984).
17. M. R. Tabrizi, S. B. Lyon, G. E. Thompson and J. M. Ferguson, *Corrosion Science,* 32, 733 (1991).
18. R. T. Foley and T. H. Nguyen, *Journal of The Electrochemical Society,* 129, 464 (1982).
19. B. Van der Linden, H. Terryn and J. Vereecken, *Journal of Applied Electrochemistry,* 20, 798 (1990).
20. J. Tedim, M. L. Zheludkevich, A. C. Bastos, A. N. Salak, A. D. Lisenkov and M. G. S. Ferreira, *Electrochimica Acta,* 117, 164 (2014).
21. M. L. Zheludkevich, K. A. Yasakau, S. K. Poznyak and M. G. S. Ferreira, *Corrosion Science,* 47, 3368 (2005).

22. B. Kuznetsov, M. Serdechnova, J. Tedim, M. Starykevich, S. Kallip, M. P. Oliveira, T. Hack, S. Nixon, M. G. S. Ferreira and M. L. Zheludkevich, *Rsc Advances,* 6, 13942 (2016).
23. C.H. Hsu and F. Mansfeld, *Corrosion,* 57 (2001).
24. B. Hirschorn, M. E. Orazem, B. Tribollet, V. Vivier, I. Frateur and M. Musiani, *Electrochimica Acta,* 55, 6218 (2010).
25. A. A. Al-Amiery, F. A. Binti Kassim, A. A. H. Kadhum and A. B. Mohamad, *Scientific Reports,* 6, 19890 (2016).
26. S. Martinez and M. Metikos-Hukovic, *Journal of Applied Electrochemistry,* 33, 1137 (2003).
27. R. Oltra, B. Vuillemin, F. Thebault and F. Rechou, *Electrochemistry Communications,* 10, 848 (2008).
28. F. Andreatta, M. E. Druart, A. Lanzutti, M. Lekka, D. Cossement, M. G. Olivier and L. Fedrizzi, *Corrosion Science,* 65, 376 (2012).
29. M. Iannuzzi, T. Young and G. S. Frankel, *Journal of the Electrochemical Society,* 153, B533 (2006).
30. K. D. Ralston, S. Chrisanti, T. L. Young and R. G. Buchheit, *Journal of the Electrochemical Society,* 155, C350 (2008).
31. B. R. W. Hinton, *Journal of Alloys and Compounds,* 180, 15 (1992).
32. T. G. Harvey, S. G. Hardin, A. E. Hughes, T. H. Muster, P. A. White, T. A. Markley, P. A. Corrigan, J. Mardel, S. J. Garcia, J. M. C. Mol and A. M. Glenn, *Corrosion Science,* 53, 2184 (2011).
33. G. Williams, A. J. Coleman and H. N. McMurray, *Electrochimica Acta,* 55, 5947 (2010).
34. S. J. Garcia-Vergara, P. Skeldon, G. E. Thompson and H. Habazaki, *Surface and Interface Analysis,* 39, 860 (2007).
35. J. D. Gorman, A. E. Hughes, D. Jamieson and P. J. K. Paterson, *Corrosion Science,* 45, 1103 (2003).

Table 1 Composition of uninhibited reference and the lithium-leaching organic model coatings.

	Non-inhibiting reference	Lithium carbonate	Lithium oxalate
Component A			
N-Butylacetate	75.0 g	75.0 g	75.0 g
Desmophen 650MPA	47.7 g	47.7 g	47.7 g
Lithium carbonate		23.6 g	
Lithium oxalate			32.0 g
Magnesium oxide		16.4 g	16.4 g
Tioxide TR 92		5.9 g	5.9 g
Blanc Fixe N ($Ba(SO_4)$)		15.4 g	15.4 g
Component B			
Tolonate HDB 75 MX	28.5 g	28.5 g	28.5 g
Dynasilan Glymo	5.2 g	5.2 g	5.2 g

Table 2 Fitted parameters for EIS spectra of the scribed coating without inhibitor after different periods of NSS exposure.

		T=0	T=2 h	T= 8 h	T=48 h	T= 168 h
EC		1	1	1	1	1
$\mathbf{R}_{sol}$	Ωcm^2	27	28	24	20	21
Q (CPE $_{Oxide}$)	$Ss^n cm^{-2}$	$1.16x10^{-4}$	$1.33\ x10^{-4}$	$1.80x10^{-4}$	$2.38x10^{-4}$	$3.50\ x10^{-4}$
$\mathbf{n}_{oxide}$		0.87	0.82	0.78	0.83	0.82
$\mathbf{R}_{oxide}$	Ωcm^2	3846	3799	3990	4506	9931
Q (CPE $_{dl}$)	$Ss^n cm^{-2}$	$4.30x10^{-4}$	$1.0\ x10^{-3}$	$1.15x10^{-3}$	$1.69\ x10^{-3}$	$2.10\ x10^{-3}$
$\mathbf{n}_{dl}$		0.85	0.90	0.92	0.89	0.95
$\mathbf{R}_{pol}$	Ωcm^2	9683	3820	6954	6591	11609
χ^2		$3.5\ x10^{-3}$	$6.0\ x10^{-3}$	$5.1\ x10^{-3}$	$4,5\ x10^{-3}$	$5.7\ x10^{-3}$

Table 3 Fitted parameters for EIS spectra of the scribed lithium carbonate loaded coating after different periods of NSS exposure.

		T=0	T=2 h	T= 8 h	T=48 h	T= 168 h
EC		1	2	2	2	2
$\mathbf{R}_{\mathbf{sol}}$	Ωcm^2	26	19	21	15	15
$\mathbf{Q(CPE}_{\mathbf{porous}}\mathbf{)}$	Ss^ncm^{-2}	-	1.30×10^{-4}	1.95×10^{-4}	1.42×10^{-5}	1.35×10^{-5}
$\mathbf{n}_{\mathbf{porous}}$		-	0.69	0.67	0.76	0.75
$\mathbf{R}_{\mathbf{Porous}}$	Ωcm^2	-	13	18	15	17
$\mathbf{Q\ (CPE}_{\mathbf{Oxide}}\mathbf{)}$	Ss^ncm^{-2}	1.06×10^{-4}	3.40×10^{-5}	2.89×10^{-5}	3.47×10^{-5}	2.82×10^{-5}
$\mathbf{n}_{\mathbf{oxide}}$		0.84	0.87	0.86	0.84	0.81
$\mathbf{R}_{\mathbf{oxide}}$	Ωcm^2	3788	9153	17009	17562	29636
$\mathbf{Q\ (CPE}_{\mathbf{dl}}\mathbf{)}$	Ss^ncm^{-2}	4.80×10^{-4}	1.76×10^{-4}	8.18×10^{-5}	5.21×10^{-5}	3.30×10^{-5}
$\mathbf{n}_{\mathbf{dl}}$		0.85	0.88	0.76	0.73	0.86
$\mathbf{R}_{\mathbf{pol}}$	Ωcm^2	12515	62248	105030	129400	237430
χ^2		3.9×10^{-3}	9.4×10^{-4}	1.1×10^{-3}	1.73×10^{-4}	7.8×10^{-4}

Table 4 Fitted parameters for EIS spectra of the scribed lithium oxalate loaded coating after different periods of NSS exposure.

		T=0	T=2 h	T= 8 h	T=48 h	T= 168 h
EC		1	2	2	2	2
$\mathbf{R}_{sol}$	Ωcm^2	26	15	15	13	13
$\mathbf{Q(CPE}_{porous}\mathbf{)}$	Ss^ncm^{-2}	-	9.31×10^{-6}	9.98×10^{-6}	1.97×10^{-5}	1.74×10^{-5}
$\mathbf{n}_{porous}$		-	0.76	0.82	0.70	0.70
$\mathbf{R}_{Porous}$	Ωcm^2	-	23	12	24	34
$\mathbf{Q(CPE}_{Oxide}\mathbf{)}$	Ss^ncm^{-2}	1.06×10^{-4}	2.11×10^{-5}	3.55×10^{-5}	3.98×10^{-5}	4.22×10^{-5}
$\mathbf{n}_{oxide}$		0.84	0.83	0.86	0.80	0.77
$\mathbf{R}_{oxide}$	Ωcm^2	3788	10775	8160	9942	37847
$\mathbf{Q\ (CPE}_{dl}\mathbf{)}$	Ss^ncm^{-2}	4.80×10^{-4}	1.54×10^{-4}	1.31×10^{-4}	2.71×10^{-5}	2.03×10^{-5}
$\mathbf{n}_{dl}$		0.85	0.72	0.70	0.82	0.97
$\mathbf{R}_{pol}$	Ωcm^2	12515	58012	42597	50748	96352
χ^2		7.1×10^{-3}	1.56×10^{-4}	2.7×10^{-4}	5.2×10^{-4}	7.4×10^{-4}

Table 5 Micro-cell data of lithium-leaching coatings after different periods of NSS exposure.

	E_{corr}/V Ag/AgCl (3M KCl)		E_{break}/V Ag/AgCl (3M KCl)			E_{corr}/V Ag/AgCl (3M KCl)		E_{break}/V Ag/AgCl (3M KCl)	
Lithium carbonate	Average	St. dev.	Average	St. dev.	**Lithium oxalate**	Average	St. dev.	Average	St. dev.
t=0	-0.47	0.04	-0.32	0.04	**t=0**	-0.51	0.04	-0.34	0.08
t =2 h	-0.27	0.03	1.49	0.30	**t =2 h**	-0.22	0.05	0.44	0.23
t= 8 h	-0.26	0.06	0.90	0.06	**t= 8 h**	-0.12	0.04	0.88	0.60
t= 48 h	-0.30	0.02	1.60	0.23	**t= 48 h**	-0.42	0.04	1.32	0.15
t= 7 days	-0.32	0.05	1.10	0.46	**t= 7 days**	-0.26	0.08	2.33	0.06

Figures:

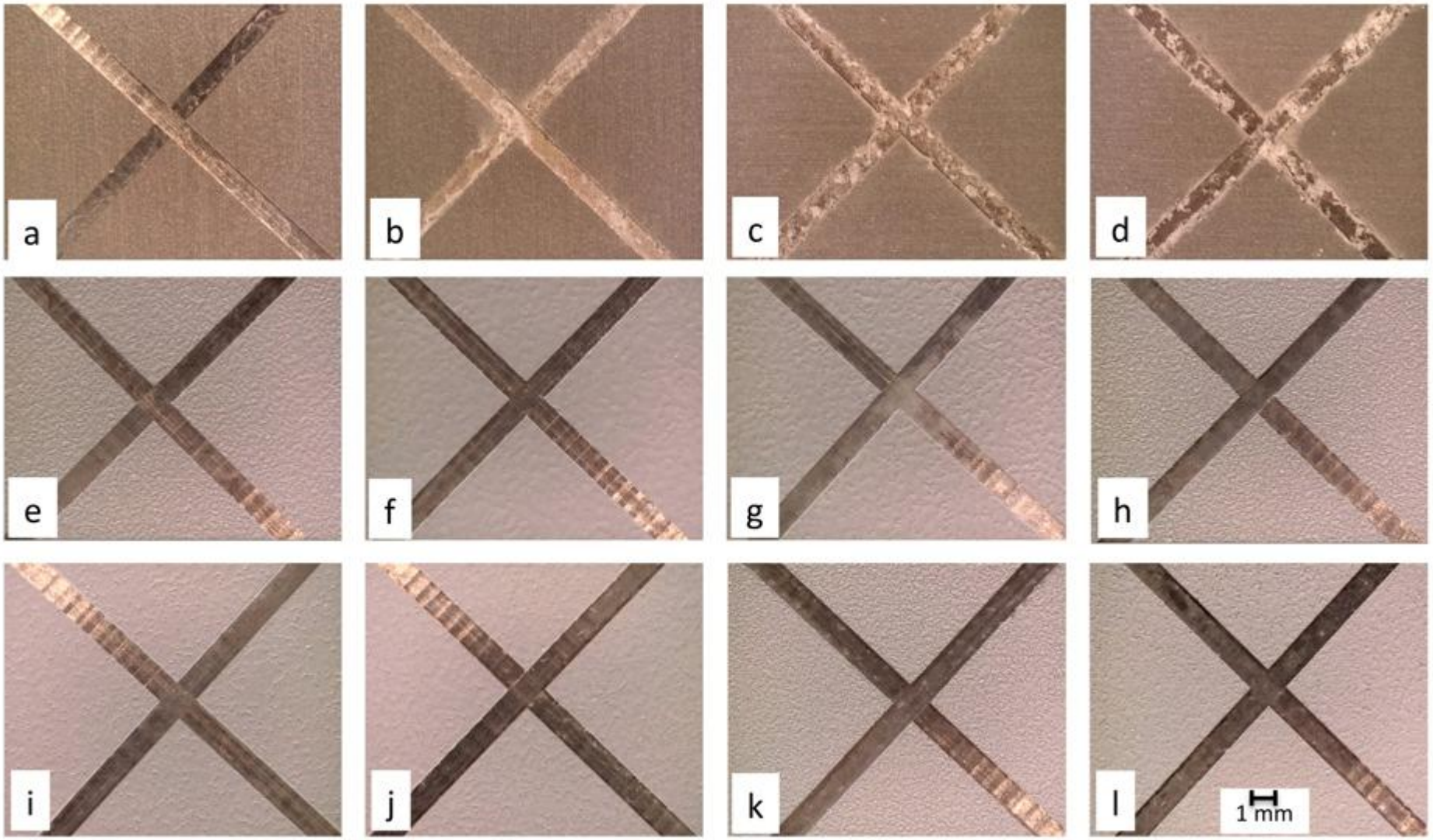

Figure 1. Top view of scribe area after neutral salt spray exposure: non-inhibited coating after (a) 2 h, (b) 8 h, (c) 48 h, and (d) 168 h; lithium carbonate doped coating after (e) 2 h, (f) 8 h, (g) 48 h, and (h) 168 h; lithium oxalate doped coating after (i) 2 h, (j) 8 h, (k) 48 h, and (l) 168 h.

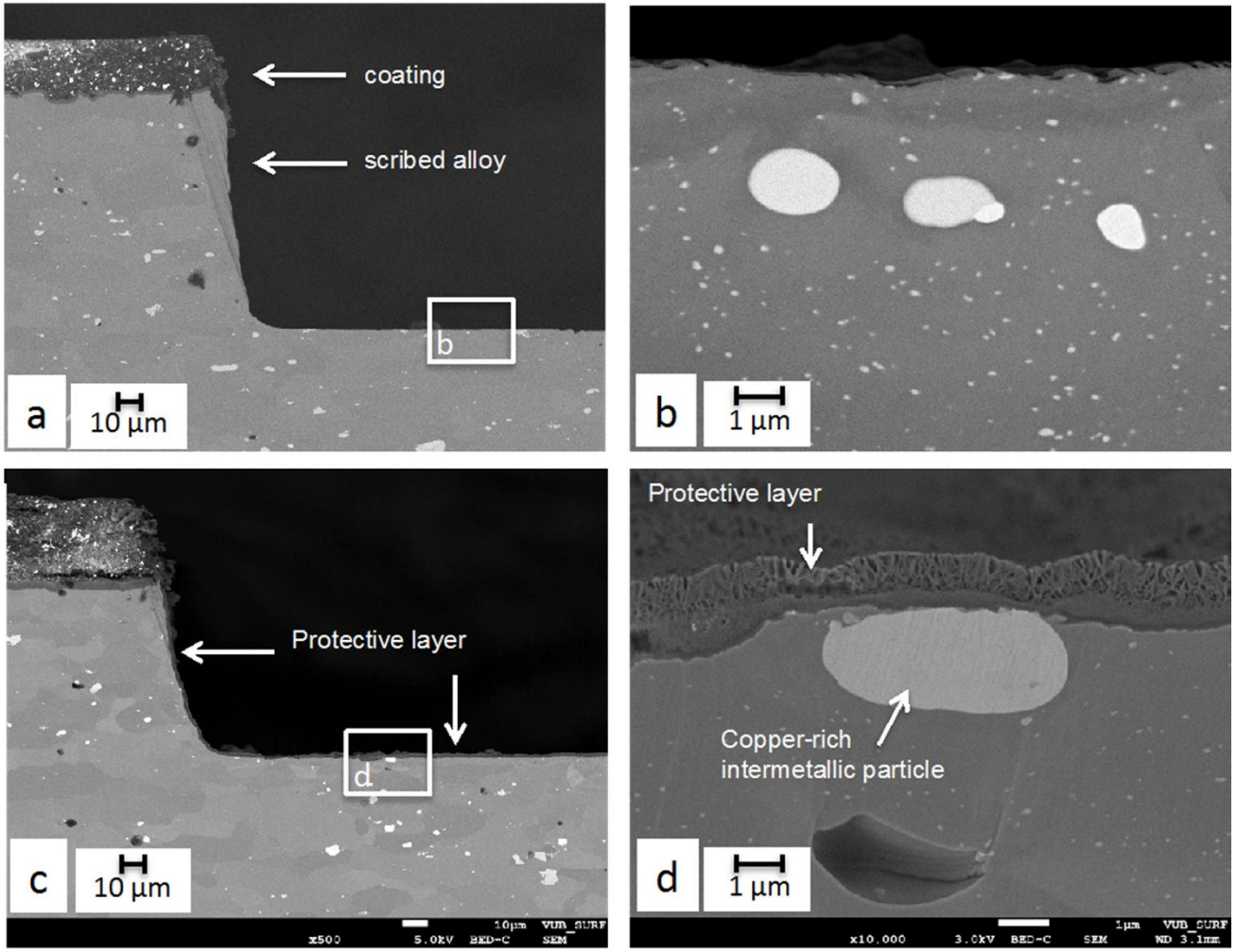

Figure 2. Microscopic cross-sectional view of the coating scribe area: (a) edge region of the defect and (b) defect bottom region before NSS exposure, and (c) edge region of the defect and (d) defect bottom region after 168 h NSS exposure for the lithium oxalate doped coating covered sample.

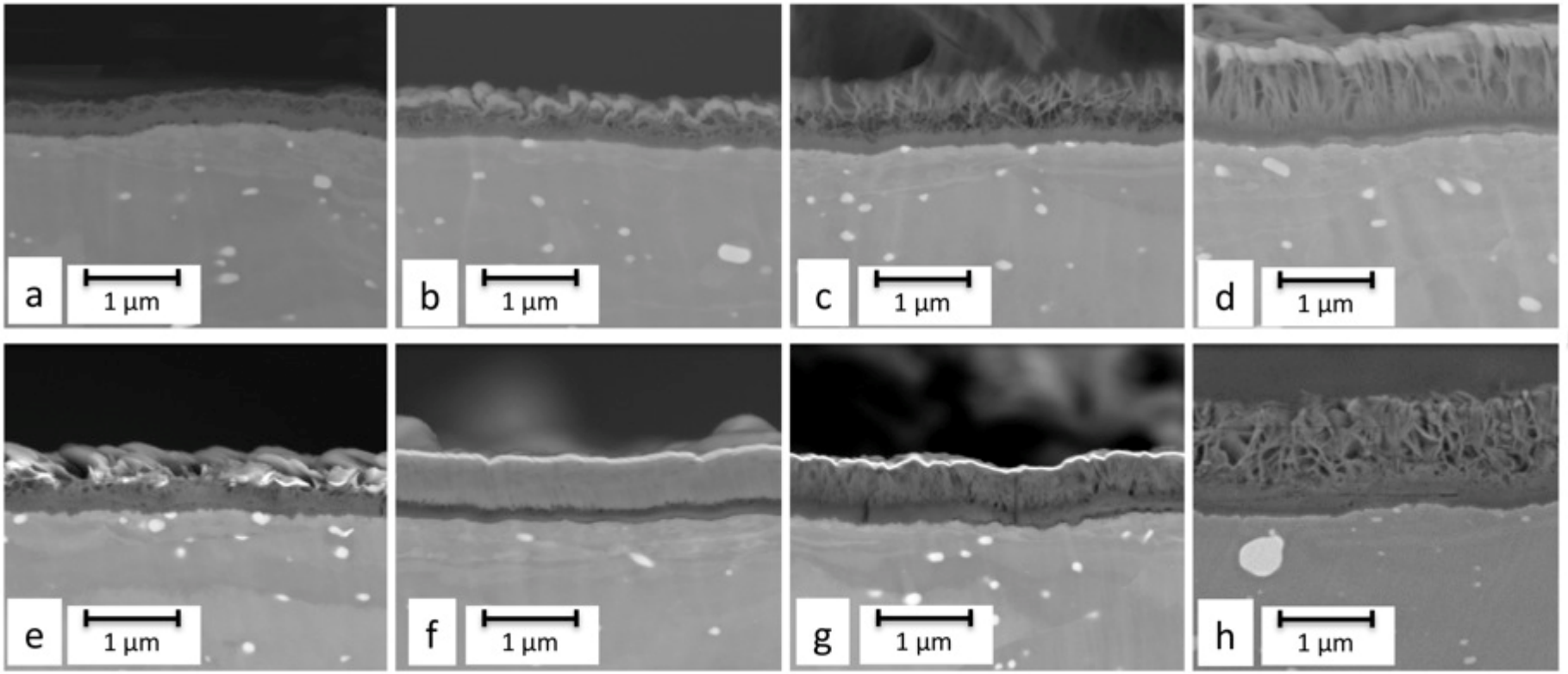

Figure 3. Cross-sectional scanning electron micrographs of the protective layer in the
scribe with time of NSS exposure: lithium carbonate doped coating after (a) 2 h, (b) 8 h, (c) 48 h, and (d) 168 h; lithium oxalate doped coating after (e) 2 h, (f) 8 h, (g) 48 h, and (h) 168 h.

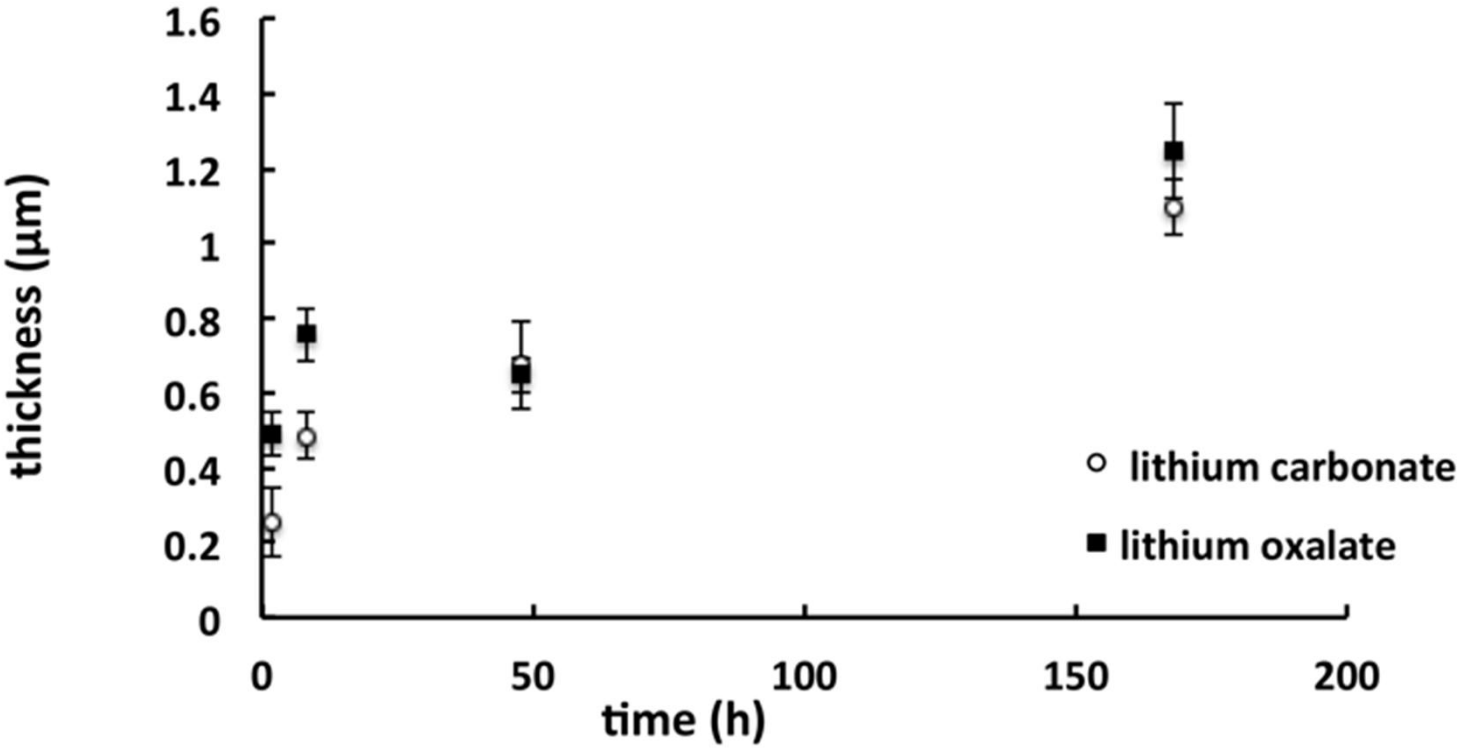

Figure 4. Measured thickness of the protective layers from lithium carbonate and lithium oxalate doped coatings over time.

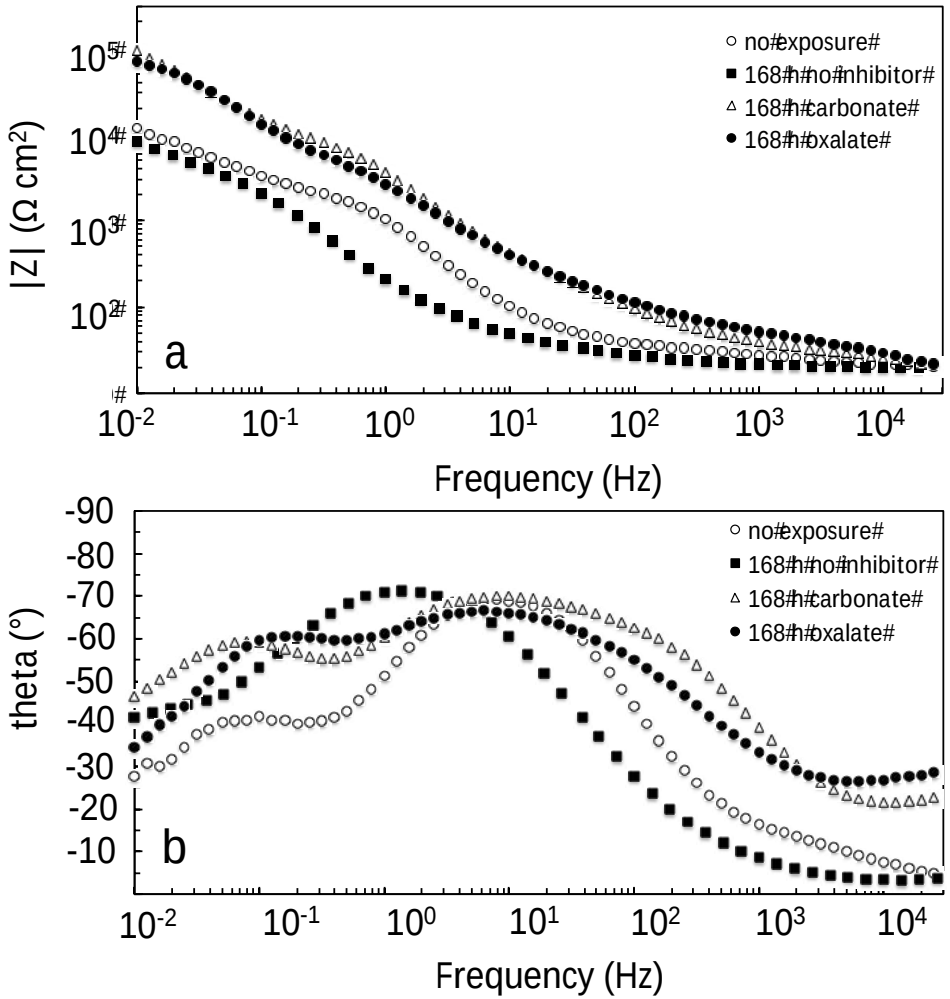

Figure 5. Electrochemical impedance spectra of the defect areas of coatings with and without lithium salts on AA2024 aluminum alloy before and after 168h NSS exposure measured with a 0.05M NaCl solution: (a) Impedance magnitude (b) phase angle plot

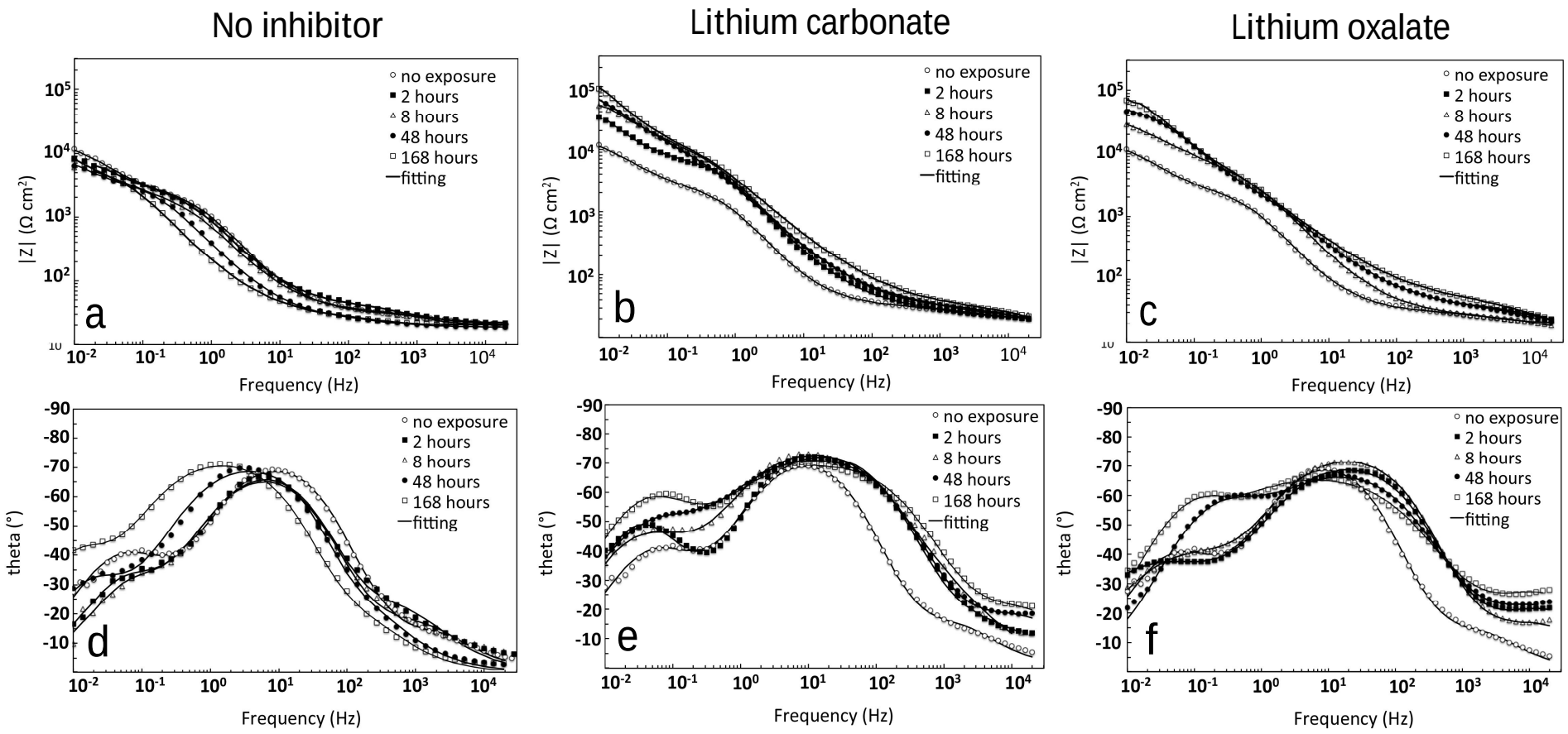

Figure 6. Electrochemical impedance spectra of the defect areas of lithium salt loaded coatings on AA2024 aluminum alloy before and after NSS exposure for 2 h up to 168 h measured with a 0.05M NaCl solution: coating with no inhibitor coating (a) Impedance magnitude (d) phase angle plot; lithium carbonate loaded coating (b) Impedance magnitude (e) phase angle plot;lithium oxalate loaded coating (c) Impedance magnitude (f) phase angle plot

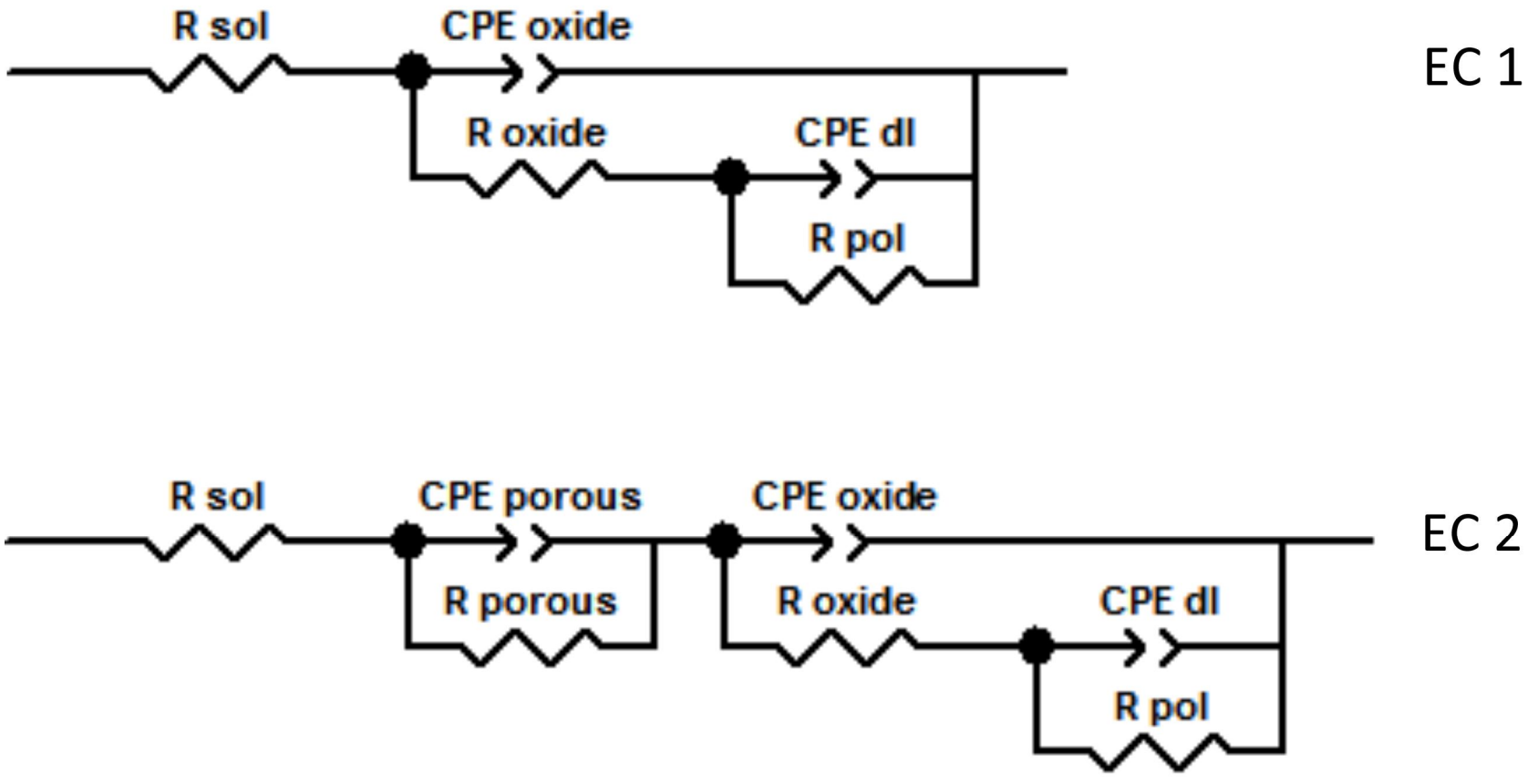

Fig ure 7. Equivalent electric circuits used to fit EIS spectra for coating defect areas: (a) EC1 for unexposed scribe and (b) EC2 for the lithium-based inhibitor generated protective layers.

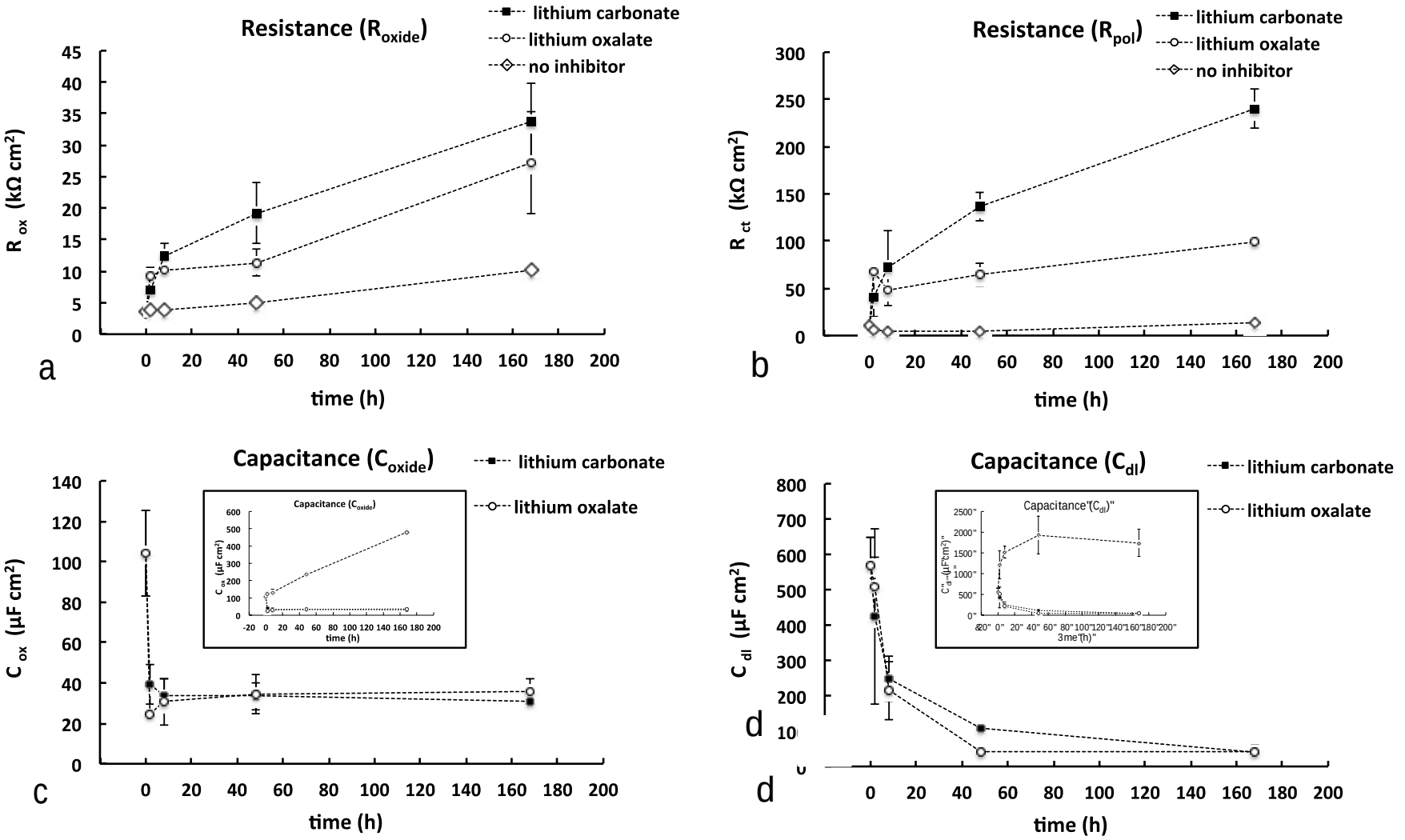

Figure 8. Evolution of (a) the dense layer resistance (R_{oxide}), (b) polarization resistance (R_{pol}), (c) dense layer capacitance (C_{oxide}), and (d) double layer capacitance (C_{dl}) after NSS exposure of scribed lithium-leaching coatings.

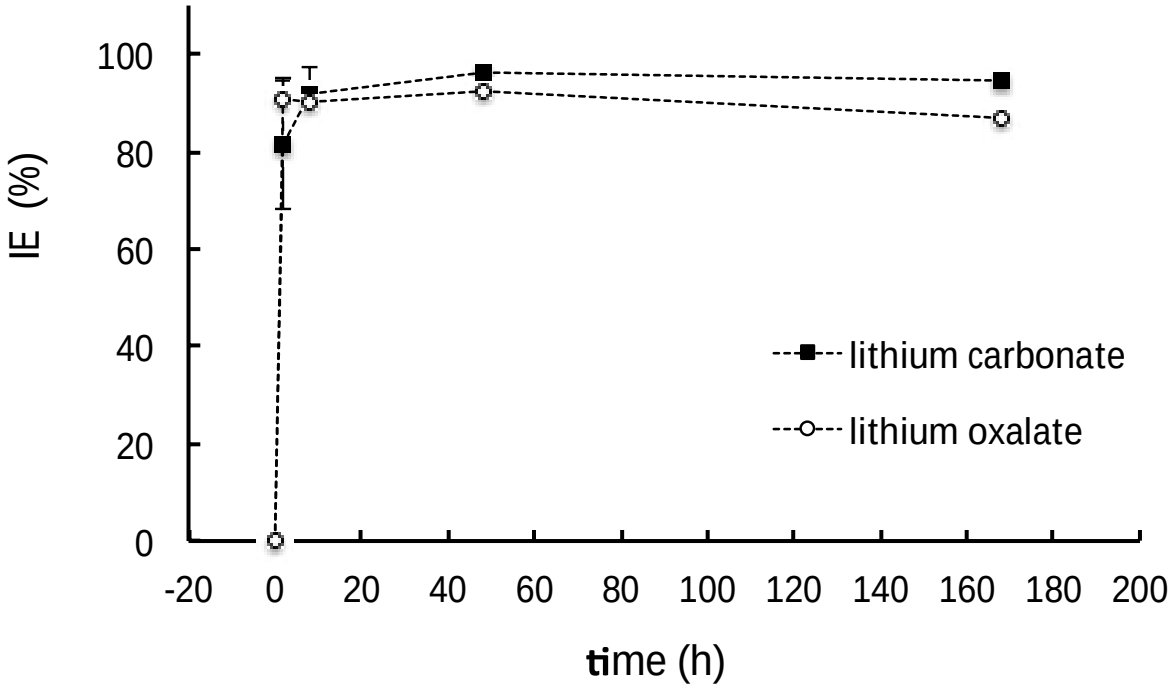

Figure 9. Evolution of inhibitor efficiency in the defect area of the lithium leaching coatings during NSS exposure.

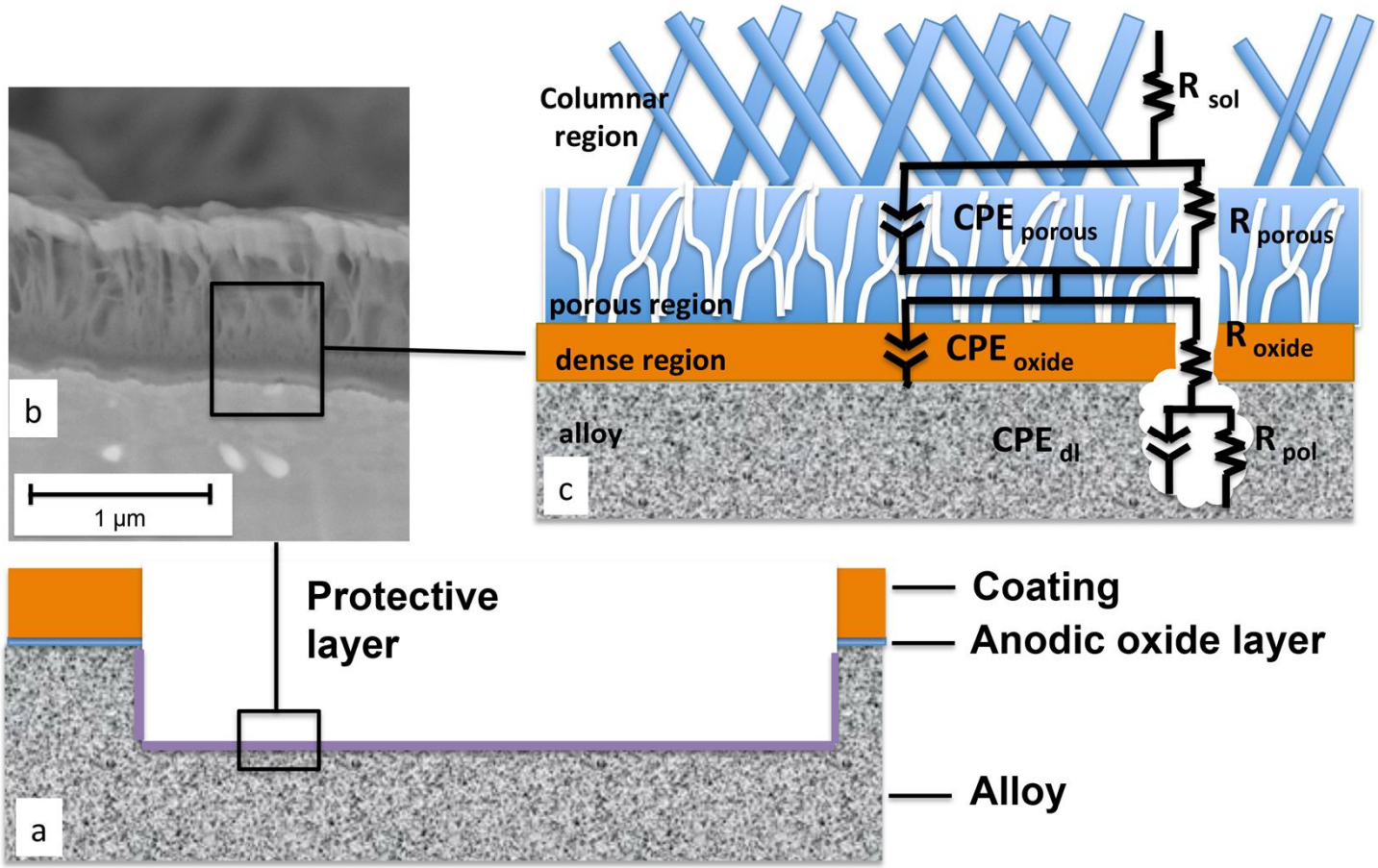

Figure 10 Schematic representation of the fitted equivalent circuit based on the physical properties of the protective layer generated in the defect from lithium-leaching organic coatings (a) the defect area with protective layer, (b) the physical coating morphology and (c) Schematic representation of EC in protective layer

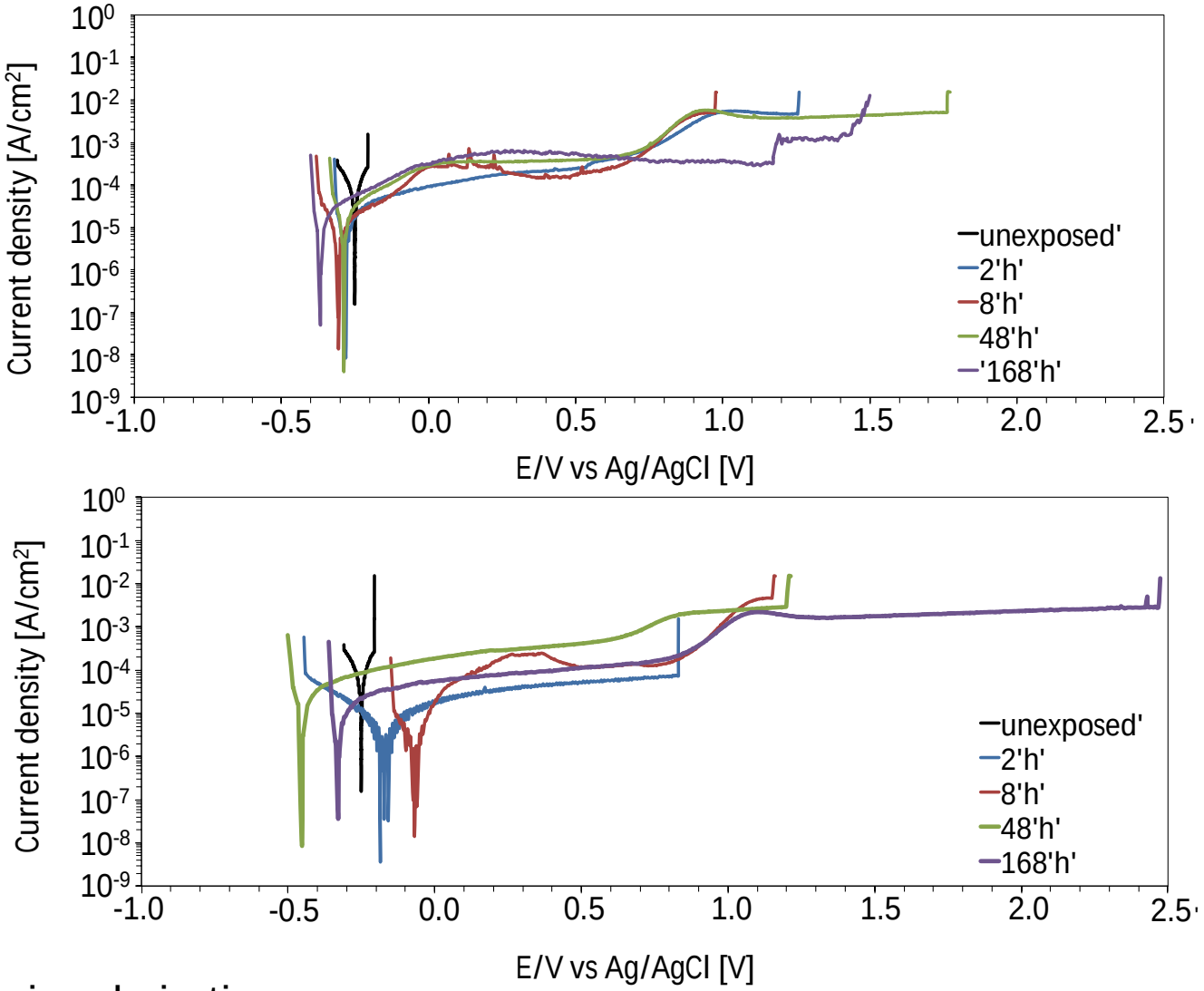

Figure 11. Potentiodynamic polarization curves in 0.05 M NaCl, solution acquired with the electrochemical micro-cell (approx. diameter 100 µm) in the defect area after NSS exposure for (a) lithium carbonate doped coatings and (b) lithium oxalate doped coatings.

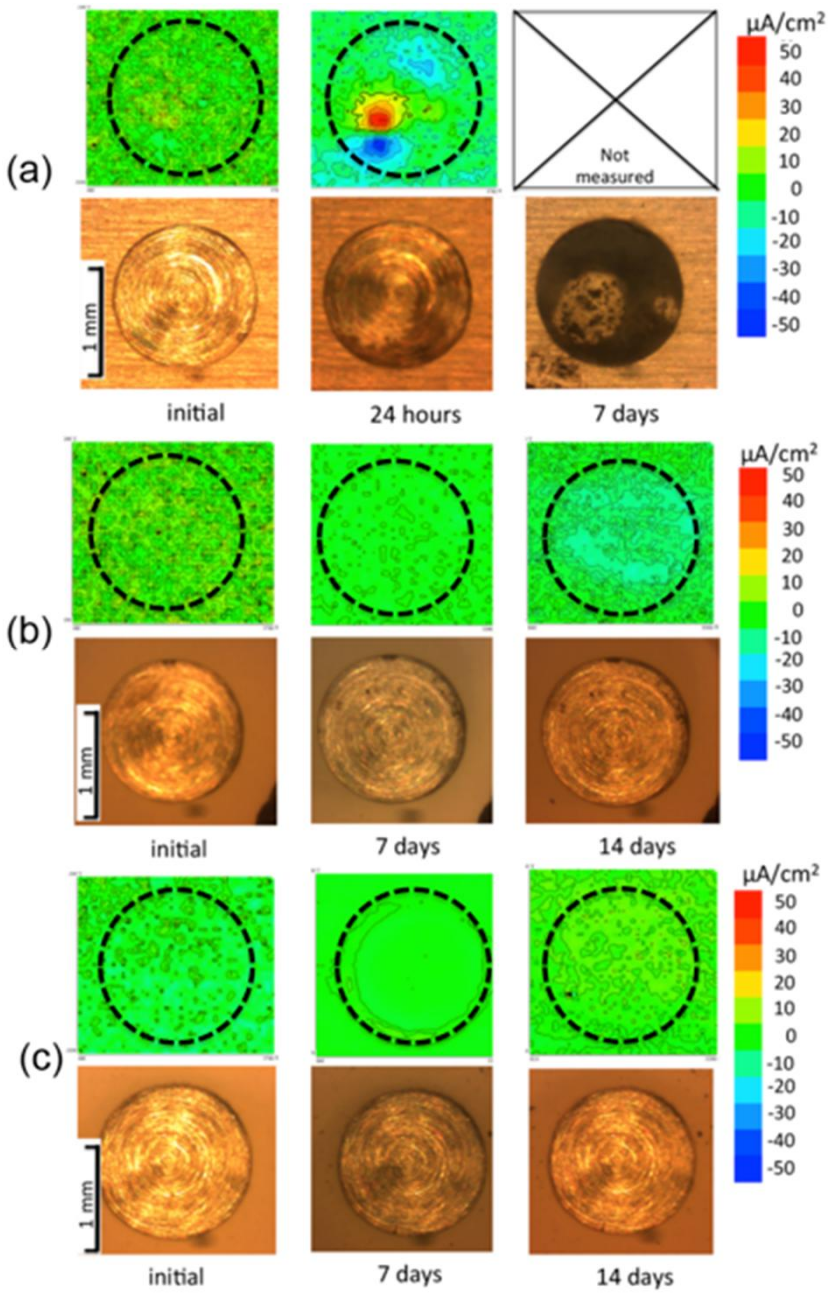

Figure 12. SVET maps to study the stability of the protective layers in a defect area immersed in 0.05M NaCl solution as a function of time: (a) uninhibited reference coating, (b) lithium carbonate coating after 168h NSS exposure, (c) lithium oxalate coating after 168h NSS exposure.